

The Tropical Oceanic Energy Budget from the TRMM Perspective. Part I: Algorithm and Uncertainties

TRISTAN S. L'ECUYER AND GRAEME L. STEPHENS

Department of Atmospheric Science, Colorado State University, Fort Collins, Colorado

(Manuscript received 22 August 2002, in final form 7 January 2003)

ABSTRACT

The earth's weather and climate is driven by the meridional transport of energy required to establish a global balance between incoming energy from the sun and outgoing thermal energy emitted by the atmosphere and surface. Clouds and precipitation play an integral role in the exchange of these sources of energy between the surface, atmosphere, and space—enhancing reflection of solar radiation to space, trapping thermal emission from the surface, and providing a mechanism for the direct transfer of energy to the atmosphere through the release of latent heat in precipitation. This paper introduces a new multisensor algorithm for extracting longwave, shortwave, and latent heat fluxes over oceans from the sensors aboard the Tropical Rainfall Measuring Mission (TRMM) satellite. The technique synthesizes complementary information from distinct retrievals of high and low clouds and precipitation from the TRMM Microwave Imager (TMI) and Visible and Infrared Scanner (VIRS) instruments to initialize broadband radiative transfer calculations for deriving the structure of radiative heating in oceanic regions from 40°S to 40°N and its evolution on daily and monthly timescales.

Sensitivity studies using rigorous estimates of the uncertainties in all input parameters and detailed comparisons with flux observations from the Clouds and Earth's Radiant Energy System (CERES) are used to study the dominant influences on the algorithm's performance and to assess the accuracy of its products. The results demonstrate that the technique provides monthly mean estimates of oceanic longwave fluxes at 1° resolution to an accuracy of $\sim 10 \text{ W m}^{-2}$. Uncertainties in these estimates are found to arise primarily from a lack of explicit vertical cloud boundary information and errors in prescribed temperature and humidity profiles. Corresponding shortwave flux estimates are shown to be accurate to $\sim 25 \text{ W m}^{-2}$, with uncertainties due to errors in cloud detection, poorly constrained cloud particle sizes, and uncertainties in the prescribed surface albedo. When viewed as a whole, the components of the method provide a tool to diagnose relationships between the climate, hydrologic cycle, and the earth's energy budget.

1. Introduction

As the actions of mankind continue to shape the environment it becomes increasingly important to understand the potential implications of these influences on the earth's climate. This, in turn, requires a thorough understanding of the physical mechanisms governing the exchange of energy between the sun, atmosphere, surface, and space required to establish a global balance between the energy that enters the earth-atmosphere system and that which leaves it. Small perturbations in any of the factors that govern this balance, whether anthropogenic or natural in origin, can lead to significant responses in the distribution and intensity of weather systems around the globe and can have profound implications for life on earth. Central to this issue is the role of the hydrological cycle governing the exchange of water between the earth's surface and atmosphere and

the interactions between the water residing in the atmospheric branch with solar and terrestrial radiation (Stephens 2002). If we are to adapt to environmental changes in the future, it is critical that we have the ability to observe small changes in the principal components of the hydrologic cycle and to predict the impact of these changes for global energy balance. This requires accurate global observations of the components that comprise the earth's energy budget (EEB) both to establish observational evidence for the equilibrium state and perturbations to it as well as to provide data with which to initialize numerical weather prediction (NWP) and climate models.

The importance of diabatic heating in the generation and maintenance of regional and global weather systems cannot be overstated. Early results from Palmén and Riehl (1957), Riehl and Malkus (1961), Yanai (1961), and Miller (1962), for example, suggested that the latent heat released in penetrative cumulus towers provides the dominant source of energy in tropical cyclones. On a larger scale, Gill (1980) demonstrated the connection between diabatic heating and the tropical circulation us-

Corresponding author address: Dr. Tristan S. L'Ecuyer, Department of Atmospheric Science, Colorado State University, Fort Collins, CO 80523.
E-mail: tristan@atmos.colostate.edu

ing a linearized model of the tropical atmosphere. Slingo and Slingo (1988, 1991) found that the magnitude and vertical distribution of longwave radiative forcing by tropical clouds plays an integral role in the location and intensity of tropical precipitation, tropical upper-tropospheric circulations, and extratropical flow patterns. Hartmann et al. (1984) demonstrated that the vertical distribution of heating significantly impacts the Walker circulation. Similar results have been documented regarding the sensitivity of the Madden-Julian oscillation (MJO) to the vertical distribution of heating (Madden and Julian 1972; Lau and Peng 1987; Takahashi 1987; Miyahara 1987; Chen and Yen 1991). Lau and Peng (1987), for example, found that the phase speed of the waves that determine the amplitude and duration of the MJO critically depends on the vertical placement of the diabatic heating maximum. The vertical distribution of heating is also expected to play a crucial role in teleconnections between tropical and midlatitude circulations such as the mechanisms by which 30–50 day oscillations are observed to manifest themselves in global phenomena (Weickmann et al. 1985; Knutson et al. 1986).

These studies demonstrate the key role that the vertical profile of diabatic heating plays in driving tropical circulations, suggesting that accurate estimates of radiative and latent heating will be invaluable in verifying their conclusions. Also, provided adequate continuity can be maintained in the data, long-term trends in the global distribution of radiative and latent heating may be well suited for monitoring global climate change. Accurate heating information can also be used to test the physical assumptions in NWP models to isolate those that perform the best. Alternatively, the information can be assimilated directly into the models through diabatic initialization (DI) or variational data assimilation. The results of Heckley et al. (1990), Puri and Davidson (1992), and Kasahara and Mizzi (1996) demonstrate that forecasts change and model spinup times decrease when diabatic heating information is included in this way. It is important to note that all of these applications require rigorous estimates of the uncertainties in the heating estimates they employ. As a result, the present work devotes equal space to developing techniques for estimating radiative and latent heating and assessing their accuracy.

There have been a number of previous studies of the radiative components of the earth's energy budget from satellites dating back to the early work of Vonder Haar and Suomi (1971). An annual mean estimate of the earth's radiation budget (ERB) and its variability deduced from satellite data was made by Stephens et al. (1981), who pointed out the importance of interannual and regional variability. The role of regional variations in cloudiness on the ERB and their feedback on the general circulation was also investigated in Hartmann and Short (1980). Results of these and a later study by Liebmann and Hartmann (1982) demonstrated a strong

correlation between features in the seasonal maps of outgoing radiation and convective cloud patterns. Arking (1991) presents an overview highlighting key findings from numerous other ERB studies prior to 1990. Since then, Randel and Vonder Haar (1990), and Sohn and Smith (1992a,b,c) have explored the interannual variability of the top of the atmosphere (TOA) radiation budget using *Nimbus-7* data. Satellite observations of TOA fluxes have recently also been used to derive short-wave radiation budgets at the the surface (Li et al. 1993; Breon et al. 1994; Ba et al. 2001a,b; Hatzianastassiou and Vardavas 2001). Furthermore, a number of recent studies have combined Earth Radiation Budget Experiment (ERBE) data with collocated cloud information in an effort to diagnose relationships between cloud properties and their impact on the TOA ERB (Stephens and Greenwald 1991a,b; Hartmann et al. 1992; Gupta et al. 1993; Ringer and Shine 1997; Moore and Vonder Haar 2001).

Recently the Clouds and the Earth's Radiant Energy System (CERES; Wielicki et al. 1996, 2001) Surface and Atmospheric Radiation Budget (SARB) working group has developed an approach to estimate TOA and surface fluxes by constraining atmospheric properties used in broadband flux calculations to agree with observed TOA fluxes (the most up-to-date information regarding SARB can be found online at: www.surf.larc.nasa.gov/surf/). Rossow and Lacis (1990), Zhang et al. (1995), Rossow and Zhang (1995), Bishop et al. (1997), and Chen et al. (2000) detail the evolution of an alternate technique that focuses first on the characterization of high and low cloud distributions from the International Satellite Cloud Climatology Project (ISCCP) and model their impact on the ERB using broadband flux calculations. While following somewhat different paths, these projects represent two of the most state-of-the-art methods for diagnosing a complete ERB to date.

This paper builds upon these earlier works with the goal of laying the foundation for improving the characterization of the principal components of the hydrologic cycle and global energy budget in oceanic regions using data from the Tropical Rainfall Measuring Mission (TRMM). The technique introduced here differs from those published previously in one or more of the following ways: 1) it addresses all components of radiation budget simultaneously and provides a rough estimate of column-integrated latent heating due to precipitation, 2) it integrates multisensor information from the state-of-the-art TRMM satellite to deduce distributions of clouds and precipitation over the tropical oceans averaged to 0.25° resolution, 3) rigorous error analyses are conducted to provide quantitative estimates of the accuracies in resulting flux estimates and highlight the dominant sources of error in each, and (4) ultimately, the resulting fluxes, collocated cloud and precipitation information, and NWP model-derived temperature and humidity fields facilitate diagnoses of cloud-radiation-climate feedbacks. The data and algorithms employed

in the approach are described in sections 2 and 3. In section 4 the algorithm is evaluated through a combination of a rigorous examination of all sources of uncertainty and a comparison with direct flux observations from CERES. This error analysis not only provides estimates of the accuracies of all flux estimates but also highlights the primary areas of deficiency with the technique from which conclusions can be drawn regarding how future observing systems may seek to better constrain the problem. Salient features of the technique are summarized in section 5. Complete analysis of the application of the algorithm to observations from the duration of the TRMM mission is left for a companion paper (L'Ecuyer and Stephens 2003, unpublished manuscript). It is anticipated that, when combined with TRMM's cloud and precipitation products, the resulting dataset will provide a tool for studying the response of the hydrologic cycle and energy budget to climate change on monthly to annual timescales.

2. Data

With TRMM, we are in a position to observe three key elements of the hydrological cycle simultaneously: water vapor, clouds, and precipitation, and their bulk radiative and electrical properties over a vast area encompassing much of the Tropics and subtropics (40°S – 40°N). This section summarizes the salient features of three distinct algorithms that make use of TRMM data to quantify the complete three-dimensional structure of clouds and precipitation over the tropical oceans.

a. Ice clouds

Cirrus clouds have a profound impact on the radiation balance of the earth–atmosphere system by virtue of their reflective properties at solar wavelengths and their absorptive properties at infrared wavelengths characteristic of terrestrial radiation (Stephens et al. 1981, 1990; Liou 1986; Sassen 2002; Stephens 2002). The relative magnitudes of these competing effects and their spatial and temporal variability represents a crucial component modulating global atmospheric circulations and must, therefore, be accounted for in any energy budget model. To this end, an algorithm is applied to infrared radiances from the Visible and Infrared Sounder (VIIRS) instrument to detect ice clouds and provide a rough estimate of their optical properties.

The cirrus cloud algorithm employed here is that of Cooper et al. (2003), which can be considered as an advanced version of the split-window technique (Inoue 1985; Prabhakara et al. 1988). The technique finds its roots in the fact that ice particles on the order of $30\ \mu\text{m}$ or smaller more efficiently absorb and emit radiation at a wavelength of $12\ \mu\text{m}$ than at $10.8\ \mu\text{m}$. As a result, cirrus clouds composed of small ice particles appear “colder” at $12\ \mu\text{m}$ than at $10.8\ \mu\text{m}$. The combination of radiances at these two channels, therefore, provides

insight into both the optical depth of the cloud and the size of its constituent particles. The optimal estimation formulation employed by Cooper et al. (2003) is well suited to the radiative budget applications in this work for two reasons. The first is the inclusion of explicit cloud boundary information in the retrieval, which is found to significantly reduce the biases inherent in traditional implementations of the approach and provides a means for determining the vertical placement of the cloud in subsequent radiative transfer calculations. Furthermore, the optimal estimation framework provides error diagnostics for all retrieved parameters often lacking in other retrievals. Such estimates are critical for assessing uncertainties in the radiative fluxes that will be derived below.

The dominant sources of uncertainty in the algorithm are due to a strong dependence on ice crystal habit, which is generally unknown, and simplifying approximations required to increase the speed of radiative transfer calculations. Expected uncertainties in each of the algorithm products—optical depth, effective radius, and cloud thermodynamic temperature—are summarized in Fig. 1. Errors in retrieved optical depth range from 20% to 40% while uncertainties in effective radius estimates typically lie between 60% and 100%. As noted in Cooper et al. (2003), the fact that optical depth is retrieved to much higher precision than effective radius is a consequence of the sensitivity of the forward model to these parameters. Estimates of cloud thermodynamic temperature are generally accurate to $\pm 7\text{ K}$ but improve substantially for colder clouds as a result of their greater impact on upwelling infrared radiances from below. These estimates are employed in a series of sensitivity studies to determine error bounds on the radiative components of the tropical energy budget in section 4a.

b. Nonprecipitating liquid clouds

In addition to the well-documented impact of ice clouds on the ERB, there have been a number of studies which suggest that water clouds have a significant impact on the global climate through strong radiative interactions (e.g., Paltridge 1980; Somerville and Remer 1984). Furthermore, using data from the *Nimbus-7* and ERBE satellites, Stephens and Greenwald (1991b) demonstrated that the response of the ERB to changes in cloud liquid water can vary substantially from region to region resulting from “gross macrophysical differences” between the clouds in disparate locations. The impact of liquid clouds on outgoing longwave radiation at the TOA is generally small (but not negligible) since they reside in the lowest levels of the atmosphere at warm temperatures relative to ice clouds and, therefore, have emission characteristics similar to the earth's surface. These clouds are, however, highly reflective and strongly influence the shortwave (SW) components of the radiation budget, particularly in the absence of high cloud. In light of these observations, we employ crude

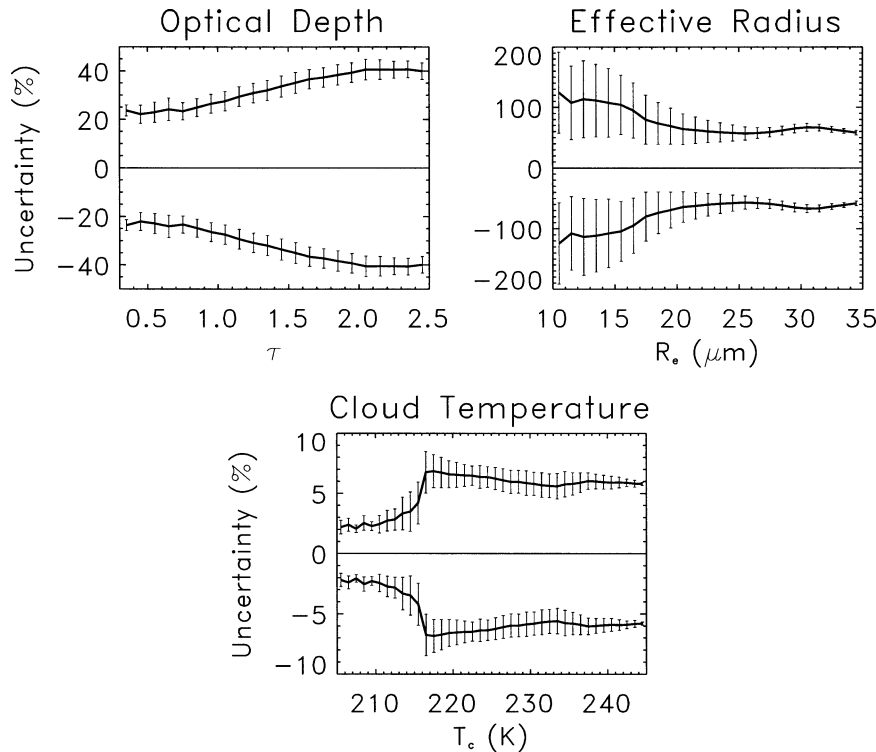


FIG. 1. Estimated uncertainty in ice cloud optical depth, effective radius, and cloud thermodynamic temperature inferred from the Cooper et al. (2003) algorithm. Solid lines correspond to mean uncertainties in all retrievals over 10 TRMM orbits while error bars represent the standard deviation about that mean for all appropriate pixels in the sample.

estimates of the location and amount of cloud liquid water in the Tropics from the passive microwave measurements available from the TRMM Microwave Imager (TMI). The resulting liquid water path (LWP) estimates and a climatologically based estimate of effective radius are then employed in the radiative transfer calculations which follow.

The method adopted for retrieving nonprecipitating liquid clouds parallels that of Greenwald et al. (1993) and is based on both horizontally and vertically polarized brightness temperatures at 19 and 37 GHz. While originally applied to retrievals from the Special Sensor Microwave Imager (SSM/I), this technique is readily adapted to the TMI as both instruments possess channels at the required frequencies. The algorithm is based on the fact that the degree of polarization of emitted microwave radiation from the ocean's surface is reduced by the absorption and reemission by water molecules and quasi-spherical liquid cloud droplets in the atmosphere before reaching the satellite. Given a model of the emission properties of a wind-roughened surface, then, one can estimate the amount of water vapor and liquid water present in the atmospheric column provided measurements of two independent polarizations at two different frequencies are available.

The liquid water path retrieval algorithm employed in the present study differs from that outlined in Green-

wald et al. (1993) in two ways. First, Greenwald et al. (1993) adjust the 37-GHz observations from the SSM/I to correct a constant offset observed in water vapor optical depth comparisons made in that study. No such correction is employed here since considerable effort has been made by the TRMM science team to ensure that the TMI radiances are well calibrated. Second, in order to determine the surface emission coefficients, $\epsilon^{H,V}$, Greenwald et al. (1993) adopt the empirical relation of Goodberlet et al. (1989) for surface wind speed as a function of 22.235-GHz brightness temperature observed by the SSM/I instrument. Since the water vapor channel on the TMI has been shifted off the center of the water vapor band to 21.3 GHz, the corresponding fit parameters are likely to be different. Rather than reparameterize this relationship using collocated TMI and buoy data, we chose to use the water vapor product of Remote Sensing Systems (RSS). [These data are obtained through the Remote Sensing Systems web site www.ssmi.com. For details of the algorithm see Wentz (1997) and Wentz et al. (2000).] These data provide high-resolution, $0.25^\circ \times 0.25^\circ$, estimates of surface wind speeds derived from the TMI observations as well as an independent estimate of column water vapor, which was used to test the performance of the present algorithm. The emissivity of the wind-roughened sur-

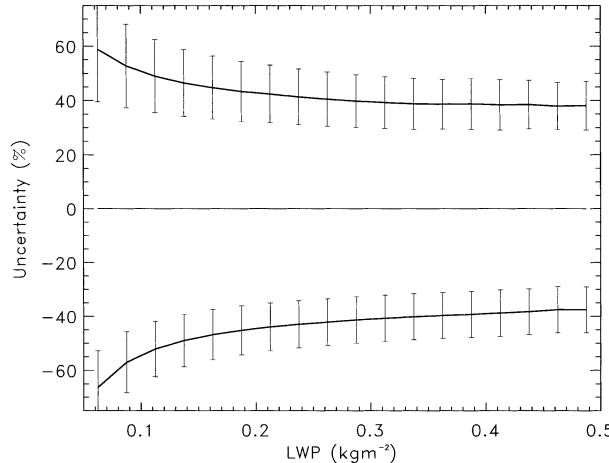


FIG. 2. As in Fig. 1 but for liquid water path estimates from the Greenwald et al. (1993) algorithm.

face is then calculated based on the model developed by Petty (1990) as in Greenwald et al. (1993).

The accuracy of retrieved liquid water paths was assessed using a series of sensitivity studies in which the two dominant factors governing the results, sea surface temperature (SST) and surface wind speed, were perturbed by amounts consistent with expected uncertainties in the RSS data. For a given set of brightness temperatures, increasing either SST or surface wind speed generally increases the estimated LWP while decreasing these quantities leads to a decrease in LWP. Average differences between baseline retrievals and LWP retrieved after both augmenting and decreasing SST by 2 K and V_{av} by 2.5 m s^{-1} establish upper and lower bounds, respectively, under the assumption that the retrieval model itself is perfect. Ultimately the uncertainty in retrieved LWP is a combination of sensitivity to SST and wind speed errors and some inherent model error. To account for this, the mean of the forward model uncertainty quoted in Greenwald et al. (1993) will be added to the component owing to uncertainties in SST and V_{av} determined previously. This approach ensures that uncertainty estimates employed in the radiative transfer calculations provide a maximum error bound on the results.

Resulting uncertainties in LWP are presented in Fig. 2. The solid lines represent the uncertainty in the LWP estimates that will be assumed in the radiative transfer calculations to follow while the error bars indicate the values one would obtain using the minimum and maximum model uncertainty quoted in Greenwald et al. (1993), 25% and 40%, respectively. The results suggest that the retrieved LWP is most sensitive to the external input at low LWP. Physically this seems reasonable since one expects the contribution of surface emission, and therefore SST and surface wind speed, to the radiation observed by the TMI to decrease as LWP increases.

A disadvantage to using passive microwave data to

infer LWP is that cloud droplets are typically much smaller than the wavelength of the radiation used, so the measurements provide little information regarding particle size. In the present study, an effective radius of $11 \mu\text{m}$ will be adopted consistent with the mean value presented in Table 1 of Miles et al. (2000), who compiled a database of in situ observations of low-level stratiform clouds made between 1972 and 1995. These values are also consistent with those quoted in Han et al. (1998). Liquid cloud vertical boundaries will be assumed to be 0.5 and 1.5 km, also based on Miles et al. (2000). A detailed analysis of the radiative implications of these assumptions, the uncertainties presented in Fig. 2, and errors in cloud detection are discussed in section 4a.

c. Precipitation

Considerable effort has been made in the past two decades to refine and improve satellite-based rainfall retrieval algorithms. The algorithms developed for TRMM represent some of the most advanced in operation, offering both estimates of surface rainfall rate as well as some information regarding the distribution of liquid and frozen hydrometeors in the entire atmospheric column. For this reason we make use of data from the TMI-based Goddard profiling algorithm (GPROF) that employs a Bayesian Monte Carlo inversion method and a database of precipitation realizations from cloud resolving model (CRM) simulations to estimate profiles of cloud and rainfall using the full complement of TMI radiances.

The GPROF algorithm, outlined in Kummerow and Giglio (1994), is performed in three steps. First, a number of cloud profiles are simulated using CRMs initialized with soundings representative of a variety of meteorological conditions. These profiles are then combined with a corresponding set of simulated TMI observations to form a very large database of scenes, which the TRMM satellite may observe as it orbits the globe. The retrieval proceeds by assigning a weight to each profile in the database depending on how closely the simulated measurements match those observed by the satellite at a given location. The final retrieved profile is a weighted sum of all the profiles in the database and consists of a surface rain rate as well as profiles of both liquid and frozen hydrometeors in 14 atmospheric layers between 0.5 and 18 km.

L'Ecuyer and Stephens (2002) have developed a model for propagating uncertainties in retrieval parameters through Bayesian retrieval algorithms and have applied it to estimate fractional uncertainties in the products of the GPROF algorithm. Omitting the mathematical details of both the algorithm and the error model for brevity, the results are summarized in Fig. 3. Uncertainties in instantaneous surface rain-rate estimates are found to range from 30% to 60% in rainfall up to 18 mm h^{-1} . In heavier rain, uncertainties rapidly increase due to the fact that all TMI channels become saturated requiring

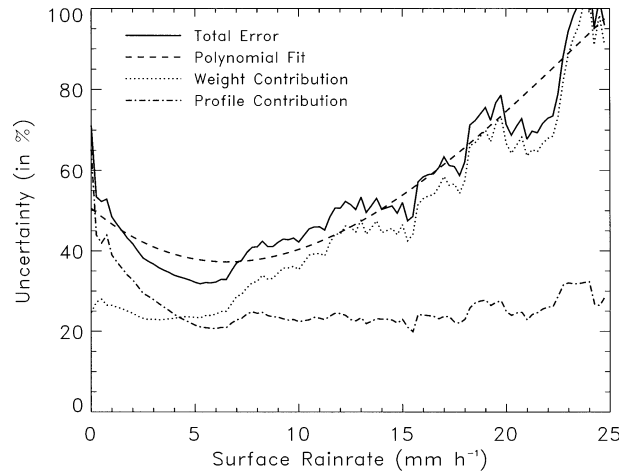


FIG. 3. Uncertainties in GPROF rainfall estimates over an oceanic background as a function of surface rain rate. Statistics have been compiled for 10 TRMM orbits.

surface rainfall to be inferred solely from the nonunique relationship between surface rain rate and the ice scattering signature in the strongly coupled 37- and 85-GHz brightness temperatures.

Errors in GPROF estimates of frozen hydrometeor concentrations are on the order of 100% while those in liquid hydrometeor concentrations generally lie between 40 and 60%. As a result, we make use of infrared radiances from the Visible and Infrared Scanner (VIRS) aboard TRMM to establish cloud-top height in precipitating regions. Assuming that precipitating clouds are optically thick, the $10.8\text{-}\mu\text{m}$ brightness temperature from VIRS is taken to be equal to the cloud-top temperature. When compared with an appropriate temperature profile it is possible to infer an effective cloud-top height above which hydrometeor water contents in all GPROF classes are set to zero regardless of that which is retrieved.

d. Background atmosphere and surface properties

In addition to clouds and precipitation, radiative flux calculations are sensitive to clear-sky atmospheric properties such as water vapor, temperature, and aerosols as well as those of the underlying surface, such as SST and surface wind speed. Since many of these properties exhibit significant spatial and temporal variability, accurate estimates of each are critical to model radiative fluxes. Profiles of temperature and moisture in the background atmosphere are obtained by matching forecasts from the European Centre for Medium-Range Weather Forecasts (ECMWF) to each TRMM overpass and interpolating the results to the vertical resolution of the GPROF rainfall profiles. Based on sensitivity studies of Eyre (1990) and Eyre et al. (1993), we anticipate uncertainties in layer temperatures and specific humidities to be approximately 2 K and 30%, respectively. The

concentrations of less variable gases such as carbon dioxide and ozone are assumed to follow the McClatchey et al. (1972) tropical atmosphere. For consistency with the other TRMM datasets used, SSTs and surface wind speeds are specified from the TMI-based RSS products. The estimated accuracies of these products are ~ 1.5 K and 2.5 m s^{-1} , respectively. (These estimates were obtained from the RSS web site www.ssmi.com/tmi/tmi_validation.html.)

Modeling the global distribution of aerosol optical properties presents a difficult challenge since both their concentrations and composition are highly variable in space and time. Satellite-based global measurements (see King et al. 1999 and references therein) are susceptible to uncertainties introduced by assumptions regarding their shape and composition, while the detailed ground-based observations of aerosol composition required to characterize their optical properties are restricted to localized regional experiments. In the present study a crude model of the global distribution of aerosols is developed from a combination of ground-based observations of their optical properties and satellite-derived estimates of their concentration. The spectral variations of aerosol extinction, asymmetry parameter, and single-scatter albedo and their vertical distributions are modeled after Toon and Pollack (1976). The integrated optical depth from this model is then scaled to agree with the mean aerosol optical depth at $0.55 \mu\text{m}$ from the Global Aerosol Climatology Project (GACP) from February 1985 through October 1988. The mean aerosol optical depth over this period is presented in Fig. 4 (top) for the oceanic regions observed by TRMM. Figure 4 (bottom) presents standard deviations over the same period providing a rough estimate of uncertainties due to temporal variability in aerosol concentrations.

It should be emphasized that this aerosol model is approximate and the error model derives simply from the statistical properties over the 4-yr period of the dataset not accounting for variability in chemical and optical properties of the aerosols at any given location. While we expect the model to be representative of average conditions, local variability in the sources and composition of aerosol particles and extreme events such as volcanic eruptions or strong dust storms are neglected. The development of accurate global aerosol models remains an open area of research so detailed analysis of such events and of the sensitivity of the results to the choice of aerosol optical properties will be left as a topic for future study.

3. The algorithm

Principal stages in the algorithm's execution are illustrated in Fig. 5. Initially GPROF surface rainfall estimates are used to discriminate between raining and nonraining pixels. Hydrometeor profiles in all pixels with nonzero rainfall rates are constructed based exclusively on the GPROF products with the VIRS constraint

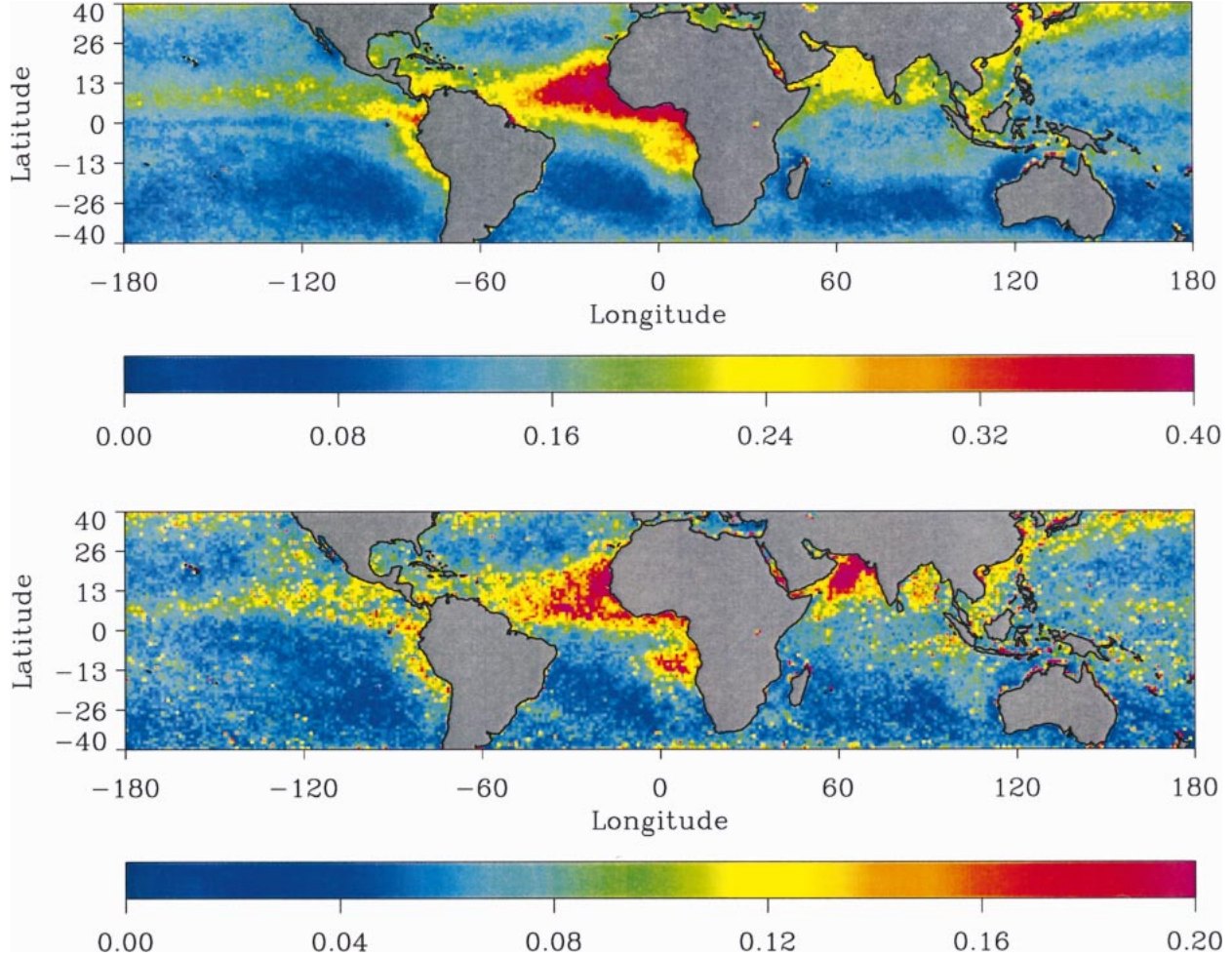


FIG. 4. (top) Mean aerosol optical depth at $0.55 \mu\text{m}$ and (bottom) its standard deviation for oceanic regions sampled by the TRMM satellite. The data represent an average over the period between Feb 1985 and Oct 1988 from the GACP aerosol climatology.

on cloud-top height. VIRS and TMI observations are used to establish the presence and properties of liquid and ice clouds in all other pixels. The results are mapped onto a uniform 0.25° grid to facilitate matching footprints of different instruments and combined with predicted profiles of temperature and humidity from ECMWF analyses and estimates of ocean surface properties from RSS to provide input to a broadband radiative transfer model to compute longwave and shortwave flux profiles for each pixel. Upwelling and downwelling fluxes at the TOA and surface are, in turn, integrated in space and time to obtain estimates of the principal shortwave and longwave components of the radiation budget and their breakdown into clear-sky and cloudy components. In addition, flux profiles are used to compute radiative heating throughout the atmospheric column and an estimate of the radiative impact of clouds at the TOA and surface. In the case of precipitating pixels, a further estimate of column-integrated latent heating is made and combined with the radiative impact of precipitating clouds.

a. Radiative transfer

Up- and downwelling broadband radiative fluxes are computed for each pixel within the cloud system making use of an implementation of the δ -two-stream approximation to the radiative transfer equation (Stephens and Webster 1979; Ritter and Geleyn 1992; Stephens et al. 2001) over 6 shortwave and 12 longwave spectral bands. The model, known as BUGSrad, is similar to that currently implemented in the Colorado State University (CSU) General Circulation Model (GCM) as well as the National Center for Atmospheric Research (NCAR) Community Climate Model (CCM). The implementation of BUGSrad used here has been modified to account for the effects of scattering, absorption, and emission from all four hydrometeor classes retrieved by GPROF using the parameterization of cloud optical properties introduced in Stephens et al. (1990). Each hydrometeor class is assumed to follow a modified gamma distribution

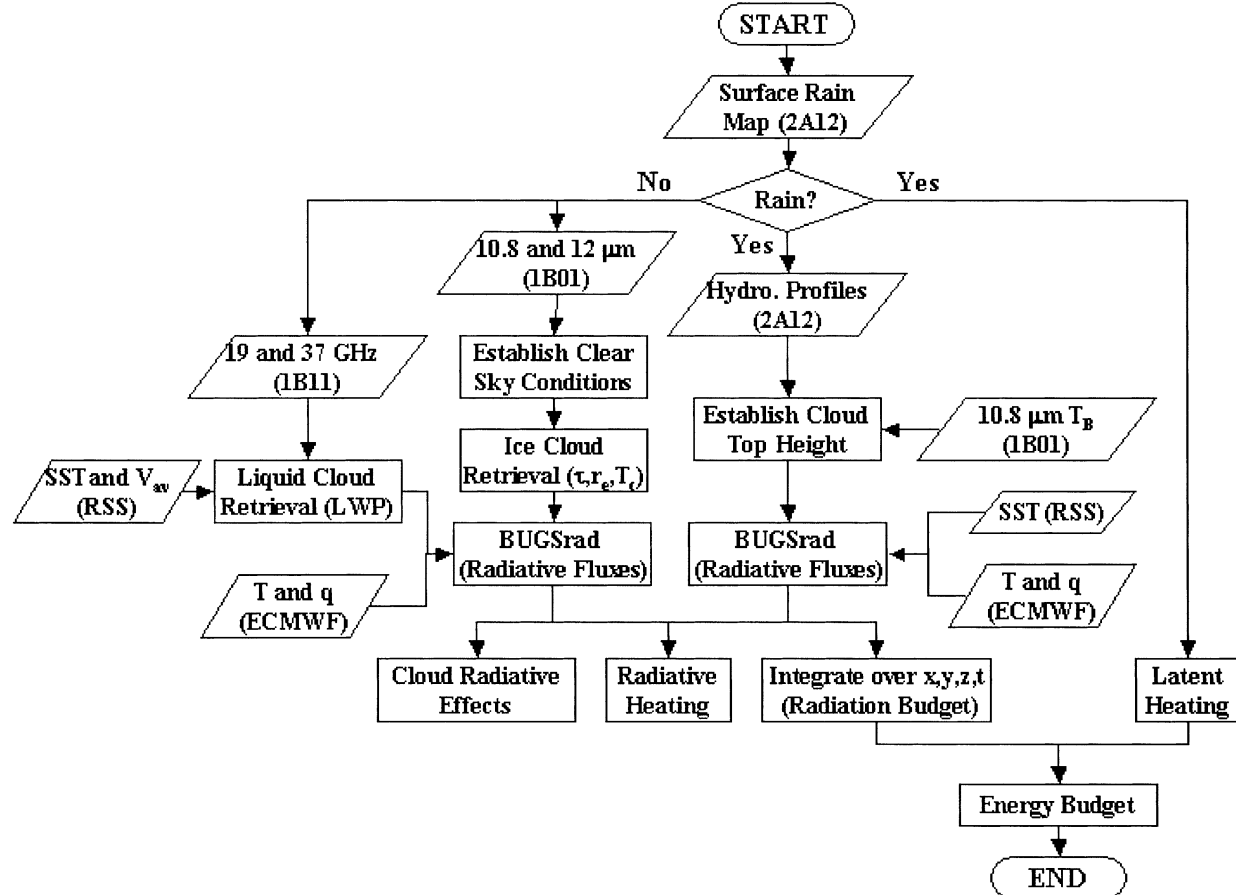


FIG. 5. Flow diagram depicting important processes and relevant sources of data at each step in the energy budget algorithm.

$$n(r) = \frac{N_0}{\Gamma(p)r_m} \left(\frac{r}{r_m} \right)^{p-1} e^{-(r/r_m)} \quad (1)$$

and the asymmetry parameter, single scatter albedo, and volume absorption and extinction coefficients are parameterized as a function of the distribution width parameter, p , and the characteristic radius, r_m . Liquid and ice clouds are assumed to follow a modified gamma distribution with $p = 2$ and characteristic radii defined by retrievals in the case of ice clouds and climatological values for liquid clouds. For consistency with the CRM simulations used in the creation of the GPROF databases, liquid and frozen precipitation hydrometeors are assumed to follow a Marshall–Palmer (Marshall and Palmer 1948) distribution with $p = 1$ and characteristic radius defined according to $r_m = 3(LWP/8\pi\rho)^{0.25}$ while liquid and ice cloud hydrometeors in precipitating pixels are taken to be monodispersed with effective radii of $100 \mu\text{m}$. The total volume concentration, N_0 , derives from the liquid or ice water content in any given layer. Gaseous absorption is treated using the correlated k -distribution formulation of Fu and Liou (1992) and surface albedo is fixed at 0.12, consistent with the ERBE-

derived mean cited in Harrison et al. (1990). A vertical resolution of 0.5 km is adopted consistent with the lowest levels of the GPROF products and the independent pixel approximation (IPA) is invoked in which each $0.25^\circ \times 0.25^\circ$ pixel is treated as radiatively isolated from its neighbors. This approximation neglects the effects of horizontal inhomogeneity within clouds and precipitation but such information has already been lost as a result of the footprint size of the instruments and the retrieval methods employed in the previous section. A series of sensitivity studies in which fluxes are recomputed calculations with various input parameters perturbed by an amount consistent with their accuracy provide error bounds on the resulting fluxes.

b. Latent heating

The cooling of the atmosphere through radiative processes is largely balanced by the release of latent heat by precipitation. This is particularly true in the Tropics, which accounts for two-thirds of global precipitation (Simpson et al. 1996). Thus some estimate of latent heating due to precipitation is required to fully char-

acterize the impact of precipitating clouds in the tropical atmosphere. When averaged over a suitably large horizontal domain, small-scale eddies in the horizontal wind components can be neglected, and the “apparent” atmospheric heat source can be written as the sum of vertical eddy flux convergence of heat, latent heating from condensation, evaporation, and sublimation, and radiative cooling (Yanai et al. 1973; Tao et al. 1993; Olson et al. 1999).

$$\begin{aligned} Q_1 = & -c_p \bar{\pi} \frac{1}{\bar{\rho}} \frac{\partial \bar{\rho} w' \theta'}{\partial z} + L_v(\bar{c} - \bar{e}) + L_f(\bar{f} - \bar{m}) \\ & + L_s(\bar{d} - \bar{s}) + \bar{Q}_R, \end{aligned} \quad (2)$$

where c , e , f , m , d , and s represent the rates of condensation, evaporation, freezing, melting, deposition, and sublimation per unit mass of air. Here, L_v , L_f , and L_s denote the latent heats of vaporization, fusion, and sublimation; $\pi = (p/1000 \text{ mb})^{R/c_p}$, R is the dry gas constant, c_p is the specific heat of air at constant pressure, θ is the potential temperature, w the vertical velocity, and p is pressure. The overbar denotes horizontal averages while the primes denote deviations from these means.

Provided a spatial and temporal domain large enough to encompass the geographic evolution and lifecycle of the cloud complex is considered, the latent heating (LH) terms can be vertically integrated from the surface to the top of the cloud to yield

$$\begin{aligned} \text{LH}_{\text{col}} = & \int_0^{z_{\text{top}}} \bar{\rho} [L_v(\bar{c} - \bar{e}) + L_f(\bar{f} - \bar{m}) \\ & + L_s(\bar{d} - \bar{s})] dz \approx \rho_i L_v R, \end{aligned} \quad (3)$$

where R is the surface precipitation rate. Thus the column-integrated LH is, in a space–time average sense, related to the total condensate removed from the system by precipitation processes since a net exchange of energy between the surface and atmosphere requires that water leave the earth's surface in the vapor phase through evaporation and reenter it in the liquid or solid phase through precipitation. Clouds that never lead to precipitation at the surface must reevaporate in the atmosphere, a process that ultimately cancels the latent heat released during their formation. This is supported by the results of Tao et al. (1993) who find that vertically integrated condensate and storm-total precipitation vary by less than 10% for modeled squall lines. Fractional uncertainties in column-integrated latent heating estimates determined in this fashion are identical to the errors in the surface rainfall estimates themselves. The most pessimistic estimate is $\sim 50\%$ assuming that the surface rainfall errors are all systematic and are not reduced through averaging over large spatial and temporal domains. A more realistic estimate, however, is 20% based on comparisons of the monthly mean rainfall products from the TMI and precipitation radar (PR) products (Kummerow et al. 2000).

To characterize the vertical structure of diabatic heating in the atmosphere more completely, one would prefer to include profiles of latent heating to complement the radiative flux profiles provided by BUGSrad. Profiles of LH, however, not only depend on profiles of condensate and water vapor but also on the dynamics of the local environment and are considerably more challenging to estimate as a result (Olson et al. 1999). The present study is, therefore, restricted to column-integrated estimates of latent heating, but a number of techniques are currently being developed for inferring latent heating profiles from TRMM observations. These methods will be incorporated into the algorithm as soon as they become available (e.g., Tao et al. 1993; Olson et al. 1999; Yang and Smith 1999a,b; 2000; Tao et al. 2001).

c. February 1998

Figure 6 illustrates mean surface rain rate from the GPROF algorithm and the fraction of TRMM observations for which the cloud retrievals indicated the presence of high and low clouds over the month of February 1998. As one would expect the largest concentrations of rainfall and cirrus clouds are associated with deep convection in the intertropical convergence zone (ITCZ) and South Pacific convergence zone (SPCZ). High clouds are also evident associated with storm tracks north of 30° , which also give rise to regions of low-level liquid cloud. Finally, persistent regions of capped stratocumulus clouds associated with subtropical highs are evident to the east of Central and South America and Africa.

These clouds and precipitation provide two important mechanisms for the exchange of energy between the surface and atmosphere. The first of these, latent heating due to all phase changes in the development of precipitation in the atmosphere from water vapor that originally evaporated at the earth's surface, is presented in Fig. 7 (top) for the month of February 1998. Since this estimate is derived following Eq. (3), the structure mimics that of the surface rainfall presented in Fig. 6 (top) tracing out the convergence zones and storm tracks. In addition to latent heating through phase changes, clouds and precipitation also modify the relative amounts of absorption and emission in the atmosphere and thus influence its total radiative heating. Figure 7 (bottom) presents the net change in column-integrated radiative heating induced by the presence of clouds and precipitation defined as the difference in net flux between the surface and TOA for all conditions minus the corresponding gflux difference in the absence of clouds and precipitation:

$$Q_{\text{rad}} = (F_{\text{SFC}}^{\text{NET}} - F_{\text{TOA}}^{\text{NET}})_{\text{all-sky}} - (F_{\text{SFC}}^{\text{NET}} - F_{\text{TOA}}^{\text{NET}})_{\text{clear}}. \quad (4)$$

The subscript all-sky refers to the observed atmosphere while clear denotes that from which all clouds and precipitation have been removed. The cloud and precipi-

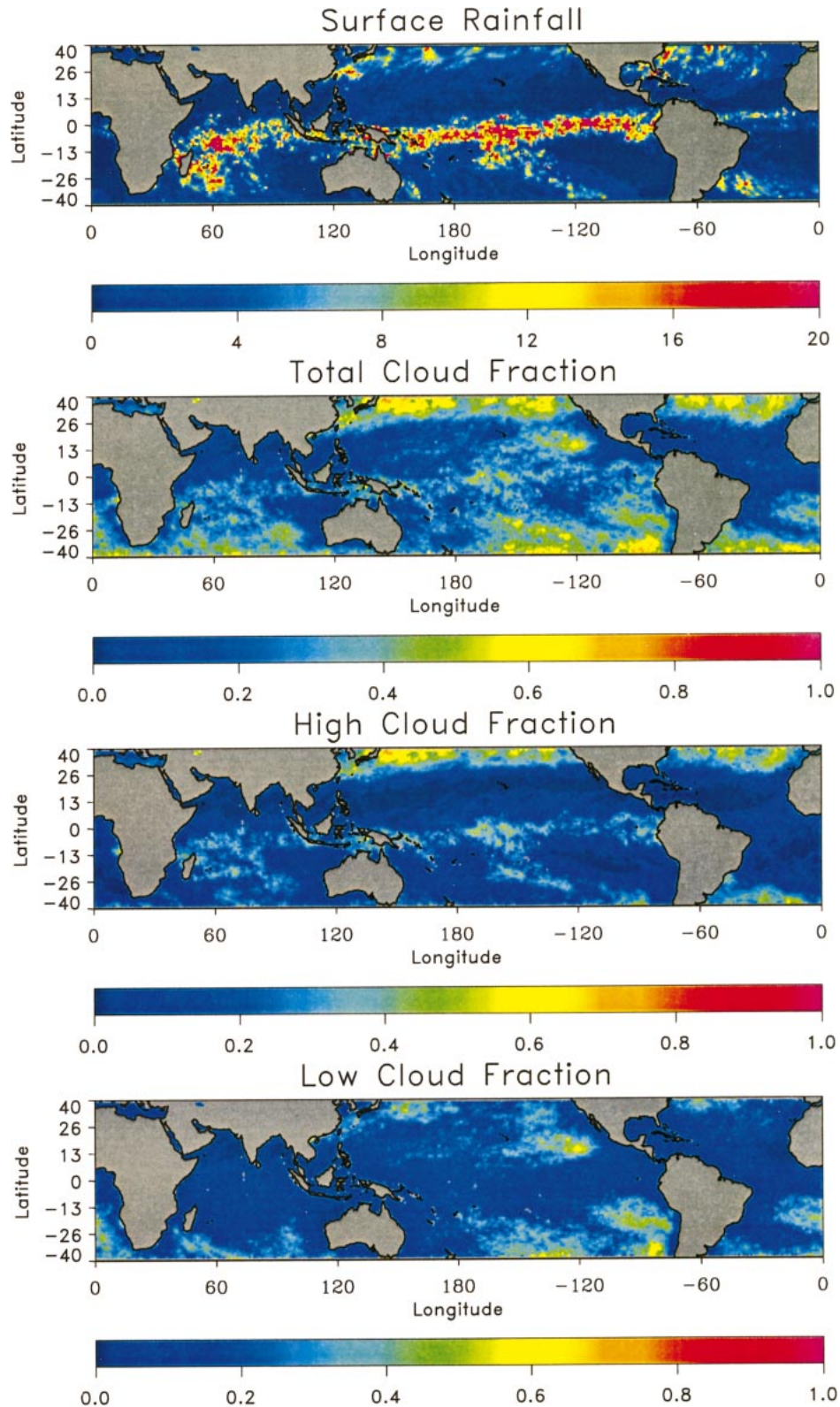


FIG. 6. (top) Mean surface rainfall rate in mm day^{-1} , and (upper middle) total cloud fraction and its breakdown into (lower middle) high and (bottom) low cloud fractions for the month of Feb 1998.

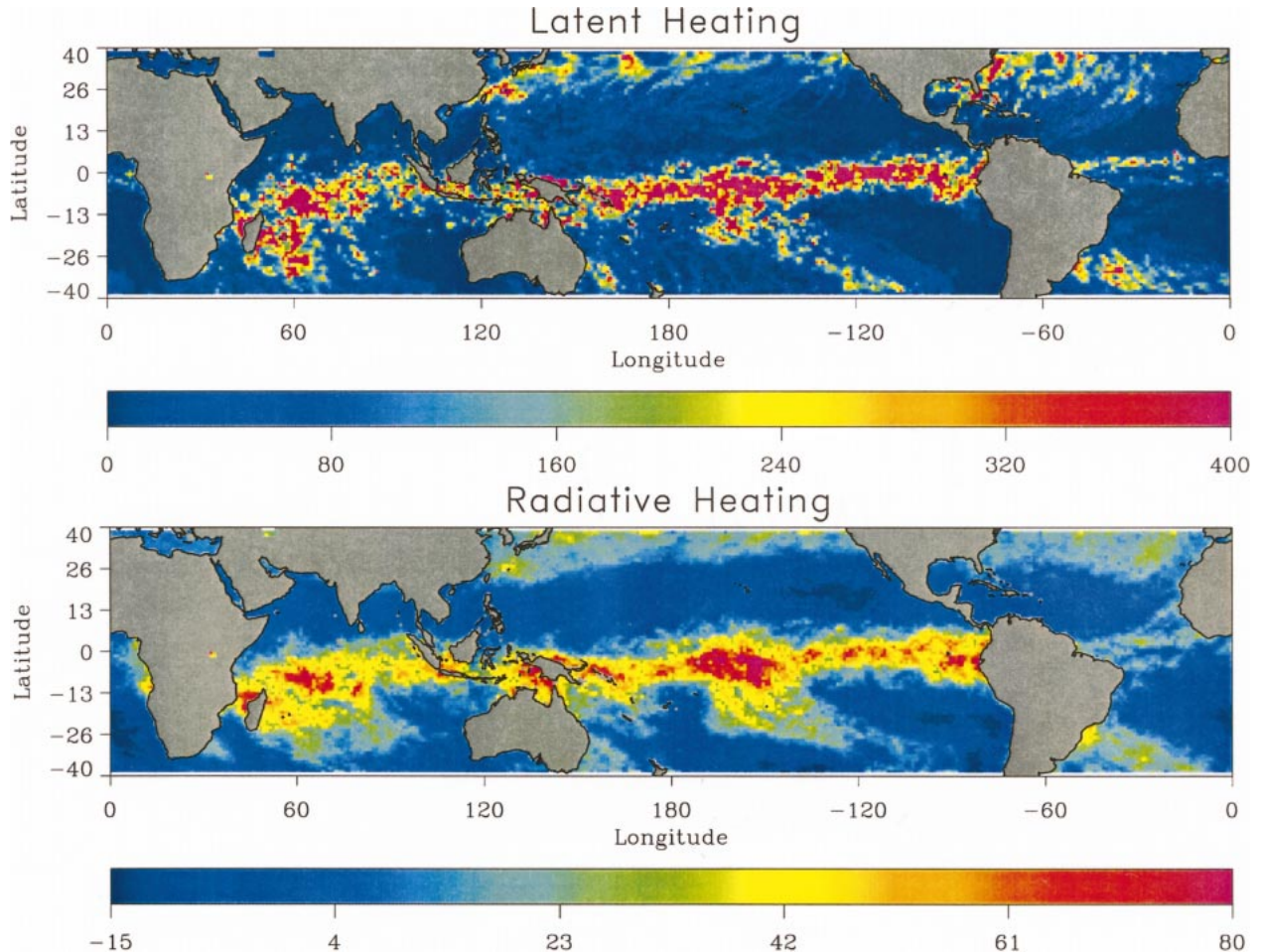


FIG. 7. (top) Monthly mean column-integrated latent heating derived from Feb 1998 mean rainfall estimates from GPROF using Eq. (3). (bottom) Cloud component of net radiative heating from BUGSrad for the same period. Both are in units of W m^{-2} .

tation components of atmospheric radiative heating is strongest in regions of prevalent high cirrus, again associated with storm tracks and convergence zones. Conversely, the capped stratocumulus clouds associated with subtropical highs have a cooling effect on the atmosphere in three large regions off the west coasts of North and South America and southern Africa. While the exception of these regions, there is a strong correlation between radiative and latent heating impacts of clouds and precipitation in the tropical atmosphere. It is important to note, however, that the physical mechanisms for radiative and latent heating from a precipitating cloud system often operate at different altitudes, thus more complete examination of their vertical distribution is required before more substantive conclusions can be drawn. This will be considered in the companion paper (L'Ecuyer and Stephens 2003, unpublished manuscript).

4. Algorithm evaluation

The performance of the algorithm has been tested using a combination of sensitivity studies and compar-

isons to TOA fluxes observed by the CERES instrument aboard TRMM. Sensitivity studies provide an invaluable tool for examining the response of the algorithm to uncertainties in the input data but make it difficult to differentiate between random and systematic errors in the model. These studies must, therefore, be complemented with comparisons against observations from other sources to develop a complete error model for the algorithm.

a. Sensitivity studies

Results of sensitivity studies detailing the impact of uncertainties in a wide variety of input parameters on longwave and shortwave fluxes at TOA and the surface are summarized in Tables 1 and 2, respectively. The first two columns in each table describe the parameter studied and the magnitude by which it is perturbed. The remaining columns summarize the impact of each perturbation on daily mean fluxes relative to the set of assumptions used in nominal implementation of the algorithm. Quoted are the deviations in mean fluxes av-

TABLE 1. Sensitivities of daily tropical mean longwave flux estimates (W m^{-2}) to uncertainties in various atmospheric properties. Corresponding rms deviations in instantaneous 0.25° fluxes are also summarized (in parentheses). The abbreviation NS indicates negligible sensitivity. Where possible a single value is used to characterize the error, but when the impact of upward and downward perturbations is asymmetric, both sensitivities have been provided separated by a slash mark.

Parameter	Perturbation	$\Delta F_{\text{LW,TOA}}^{\uparrow}$	$\Delta F_{\text{LW,SFC}}^{\uparrow}$	$\Delta F_{\text{LW,SFC}}^{\downarrow}$
Atmospheric and surface properties				
Water vapor profile	$\pm 30\%$	∓ 4.9 (5.5)	NS	± 12.8 (14.4)
Water vapor (> 500 hPa)	$\pm 30\%$	∓ 2.1 (2.4)	NS	± 0.1 (0.1)
Water vapor (< 500 hPa)	$\pm 30\%$	∓ 2.8 (3.2)	NS	± 12.7 (14.3)
Atmospheric temperature	± 2 K	∓ 5.0 (5.7)	NS	± 1.8 (2.1)
Surface albedo	± 0.03	NS	NS	NS
Sea surface temperature	± 2 K	∓ 1.3 (1.6)	± 10.1 (10.8)	± 6.0 (6.3)
Aerosol	$\pm 1 \sigma$	∓ 0.3 (0.4)	NS	NS
Ice cloud properties				
Ice water path	$\pm 30\%$	∓ 1.7 (3.5)	NS	± 0.1 (0.3)
Effective radius	$\pm 60\%$	∓ 2.7 (5.6)	NS	∓ 0.2 (0.5)
Thermodynamic temperature	± 7 K	∓ 2.4 (5.0)	NS	± 0.2 (0.5)
Geometric thickness	∓ 1 km	∓ 0.9 (1.9)	NS	± 0.1 (0.4)
Detection threshold	$T_{B,10.8_{\text{max}}} \pm 5$ K	∓ 1.6 (4.5)	NS	± 0.1 (0.4)
Nonprecipitating liquid cloud properties				
Liquid water path	$\pm 40\%$	NS	NS	NS
Effective radius	$18/7 \mu\text{m}$	$0.1(0.3)/-1.2(2.5)$	NS	$-0.1(0.1)/0.2(0.4)$
Cloud height	5.0/0.5 km	$-2.3(4.8)/0.9(1.9)$	NS	$-0.8(1.6)/3.2(5.6)$
Geometric thickness	3.5/0.5 km	$-0.9(1.9)/0.3(0.7)$	NS	$2.2(3.8)/\text{NS}$
Detection threshold	$LWP_{\text{min}} \pm 0.025 \text{ kg m}^{-2}$	$-1.7(2.9)/0.9(1.7)$	NS	$4.8(8.9)/-2.7(6.1)$
Precipitating cloud properties				
Ice water path	$\times/\div 2.0$	∓ 0.3 (0.8)	NS	NS
Liquid water path	$\times/\div 1.5$	NS	NS	± 0.1 (0.3)

eraged over the oceanic domain between 40°N and 40°S , while the quantities in parentheses correspond to root-mean-square (rms) differences in individual pixels at 1.0° resolution. Since a majority of the pixels sampled by TRMM are observed only 1 time per day, the rms differences isolate the average contribution of each input parameter to the uncertainty in flux estimates at pixel resolution, while the tropic-mean differences indicate the expected order of magnitude of biases that could result in daily radiation budget estimates due to systematic errors in the input parameters. Note that downwelling fluxes at TOA are omitted from these tables as they are not sensitive to any of the input parameters. We assume that solar insolation is known to accuracies of $\sim 0.5 \text{ W m}^{-2}$ from measurements by active cavity radiometers [e.g., the Active Cavity Radiometer Irradiance Monitor (ACRIM) instrument described in Willson (1984)] while incoming longwave radiation is negligible.

Table 1 suggests that longwave fluxes are most susceptible to errors in profiles of temperature and humidity by virtue of their role in both clear and cloudy pixels. Systematic perturbation of either field leads to errors of 5 W m^{-2} in outgoing longwave radiation (OLR). Interestingly, the impact of water vapor on OLR is equally distributed between that above and below 500 hPa despite the fact that less than 10% of the total atmospheric water vapor mass resides above 500 hPa. The other important source of uncertainty in OLR is the distribution of ice cloud microphysical properties. At the in-

dividual pixel level errors in retrieved effective radii and thermodynamic temperatures of ice clouds can lead to errors of as much as 90 W m^{-2} in estimates of OLR but typically result in biases of $2\text{--}3 \text{ W m}^{-2}$ when averaged with all noncloudy pixels over the entire TRMM domain. Downwelling longwave fluxes at the earth's surface are most sensitive to errors in water vapor at levels below 500 hPa that introduce uncertainties of up to 13 W m^{-2} . A secondary source of error is the uncertainty in sea surface temperature that can lead to a bias of as much as 6 W m^{-2} when integrated over the whole domain. The sole contribution to uncertainties in upwelling longwave fluxes from the surface arises from errors in specified SSTs, which lead to errors of $\sim 10 \text{ W m}^{-2}$.

Table 2 demonstrates that uncertainties in shortwave fluxes are dominated by errors in surface albedo and in the retrieved distribution of liquid clouds and their microphysical properties. In individual pixels, uncertainties in LWP and effective radius often lead to errors in outgoing shortwave radiation (OSR) and downwelling shortwave fluxes at the surface on the order of 100 W m^{-2} . Averaging with surrounding clear-sky pixels reduces their impact to $4\text{--}8 \text{ W m}^{-2}$. Systematic errors in the assumed surface albedo lead to errors of 9 W m^{-2} in the reflected solar radiation from the earth's surface. After some attenuation these errors lead to a 7 W m^{-2} error in OSR. Finally, as a result of the absorption of shortwave radiation by water vapor, errors in the specification of water vapor concentrations below 500 hPa

TABLE 2. As in Table 1 but for monthly mean shortwave flux estimates.

Parameter	Perturbation	$\Delta F_{\text{SW,TOA}}^{\uparrow}$	$\Delta F_{\text{SW,SFC}}^{\uparrow}$	$\Delta F_{\text{SW,SFC}}^{\downarrow}$
Atmospheric and surface properties				
Water vapor profile	$\pm 30\%$	∓ 0.8 (1.4)	∓ 0.4 (0.7)	∓ 3.8 (6.2)
Water vapor (>500 hPa)	$\pm 30\%$	∓ 0.1 (0.2)	NS	∓ 0.1 (0.2)
Water vapor (<500 hPa)	$\pm 30\%$	∓ 0.7 (1.3)	∓ 0.4 (0.7)	∓ 3.7 (6.0)
Atmospheric temperature	± 2 K	∓ 0.1 (0.4)	NS	∓ 0.2 (0.6)
Surface albedo	± 0.03	∓ 7.4 (12.3)	∓ 9.0 (14.8)	± 1.0 (1.9)
Sea surface temperature	± 2 K	NS	NS	NS
Aerosol	$\pm 1 \sigma$	∓ 0.5 (0.9)	∓ 0.1 (0.1)	∓ 0.5 (1.0)
Ice cloud properties				
Ice water path	$\pm 30\%$	∓ 0.9 (4.1)	∓ 0.1 (0.5)	∓ 1.0 (4.5)
Effective radius	$\pm 60\%$	∓ 1.6 (7.3)	∓ 0.2 (0.8)	± 1.6 (7.0)
Thermodynamic temperature	± 7 K	∓ 0.2 (1.3)	NS	± 0.2 (1.4)
Geometric thickness	2/1 km	∓ 0.1 (0.7)	NS	± 0.1 (0.7)
Detection threshold	$T_{B,10.8_{\text{max}}} \pm 5$ K	∓ 0.3 (1.8)	NS	∓ 0.4 (2.2)
Nonprecipitating liquid cloud properties				
Liquid water path	$\pm 40\%$	∓ 3.6 (11.6)	∓ 0.5 (1.7)	∓ 4.3 (14.1)
Effective radius	$18/7 \mu\text{m}$	∓ 7.0 (22.0)	∓ 0.9 (2.9)	± 7.6 (24.6)
Cloud height	5.0/0.5 km	∓ 1.7 (5.2)	NS	∓ 0.5 (1.9)
Geometric thickness	3.5/0.5 km	NS	NS	NS
Detection threshold	$LWP_{\text{min}} \pm 0.025 \text{ kg m}^{-2}$	11.6(31.9)/ $-7.7(26.0)$	$-1.7(4.7)/-1.1(3.9)$	$-14.3(74.8)/9.5(32.4)$
Precipitating cloud properties				
Ice water path	$\times/\div 2.0$	∓ 0.5 (3.3)	∓ 0.1 (0.5)	∓ 0.8 (4.6)
Liquid water path	$\times/\div 1.5$	∓ 0.2 (0.8)	NS	∓ 0.3 (1.3)

can also lead to errors of up to 4 W m^{-2} on the downwelling shortwave radiation at the surface.

Perhaps surprisingly, the impact of uncertainties in precipitating regions on tropical mean fluxes is negligible. This is primarily a result of the fact that, on average, raining pixels account for less than 10% of the domain considered and thus do not impact the averages much. It should be noted that at the pixel level, however, errors in shortwave fluxes often exceed 50 W m^{-2} . Conversely, errors in longwave fluxes seldom exceed 10 W m^{-2} due to the fact that the clouds associated with precipitation are optically thick and their impact on longwave fluxes has saturated in many cases. In fact, rms errors in shortwave fluxes at the pixel level (in parentheses in Tables 1 and 2) are generally much larger than errors determined by comparing tropical means in all cases involving cloud and precipitation properties. Many of the dominant sources of uncertainty in longwave fluxes, such as atmospheric temperature and water vapor, have a more or less uniform effect from pixel to pixel. As a result, pixel-scale rms errors in longwave flux estimates, on the other hand, are generally very similar to those determined from the tropical means. The dominant sources of error in shortwave fluxes, such as liquid water path and effective radius, are strongly dependent on the characteristics of the scene being viewed. This, coupled with the diurnal cycle of solar radiation at the top of the atmosphere leads to greater pixel-to-pixel variability in the resulting errors. Thus, at the individual pixel level we anticipate larger uncertainties in shortwave than longwave fluxes but comparable uncertainties in TRMM domain-average fluxes.

In addition to the sources described earlier, it is important to characterize the impact of errors in cloud detection, a problem encountered in most passive remote-sensing techniques. This has been modeled by varying the LWP and brightness temperature thresholds by which liquid and ice clouds are identified. The results demonstrate that accurate detection of liquid clouds is extremely important for modeling shortwave fluxes in the atmosphere. Failure to model a liquid cloud can lead to errors in OSR and downwelling shortwave fluxes at the surface exceeding 200 W m^{-2} . Equivalently, false detection of a cloud leads to uncertainties of equal magnitude but in the opposite direction. When averaged over the TRMM domain, systematic errors in liquid cloud detection lead to uncertainties of $10\text{--}15 \text{ W m}^{-2}$ in shortwave fluxes and represent the largest single error source on these estimates. A solution to this problem may come in the form of a multisensor technique that combines visible radiances from VIRS with the TMI microwave radiances such as that introduced by Masunaga et al. (2002). While this approach is only applicable during the daytime, it may be supplemented with the microwave-only technique at night since longwave fluxes are much less sensitive to errors in cloud detection.

Errors introduced by misrepresentation of ice clouds is small by comparison primarily due to the fact that all errors are restricted to the identification of extremely thin cirrus clouds (IR optical depths less than 0.2). At the individual pixel level these clouds can lead to errors of as much as 50 W m^{-2} in OLR but when integrated over the entire oceanic TRMM sampling domain, their effect is on the order of 2 W m^{-2} . This result is con-

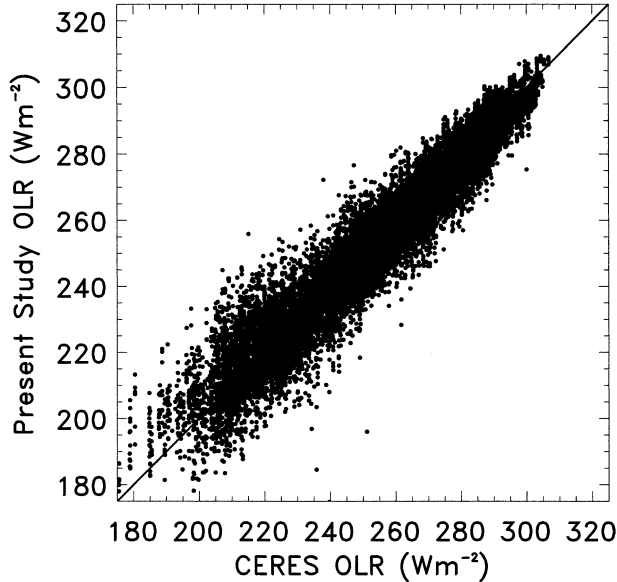


FIG. 8. Comparison of OLR from the present study to that observed by the CERES instrument aboard TRMM. Each data point corresponds to the Feb 1998 mean OLR for a single 1.0° grid box over the oceanic portion of the TRMM domain.

sistent with the fact that the algorithm used to infer cirrus cloud microphysical properties is explicitly designed to detect thin cirrus clouds (Inoue 1985; Prabhakara et al. 1988).

It should be noted that the error estimates provided in Tables 1 and 2 apply only to fluxes at atmospheric boundaries. Uncertainties in corresponding vertical flux profiles are likely to be much larger due to the inherent difficulties in extracting cloud boundary information from passive observations. Analyses of the vertical structure of radiative heating in the atmosphere using this technique should, therefore, be restricted to a few coarse atmospheric layers even though flux profiles are computed at a vertical resolution of 0.5 km. Furthermore, there exist a number of additional sources of uncertainty that have not been addressed here. These include errors due to temporal and spatial sampling, the sensitivity of the results to subpixel variability in cloud and precipitation fields, and errors due to the radiative transfer model itself such as parameterizations of cloud optical properties the aerosol model adopted. Evaluation of the impact of these error sources requires a more rigorous treatment and are topics of ongoing research.

b. External validation

In climate study applications involving long-term and wide-area means or in variational data assimilation where accurate observational covariance matrices are required, random errors must be distinguished from biases. While the results of the previous section demonstrate the sensitivity of the algorithm to errors in the input, it is not possible to separate random and system-

TABLE 3. Correlation, rms differences, and biases between monthly mean outgoing longwave and shortwave radiation estimates at 1.0° resolution from the present study, the CERES ES-9 product, and the NOAA Interpolated OLR product.

	Correlation	Rms difference	Bias
CERES OLR	0.966	7.07 W m^{-2}	-0.88 W m^{-2}
CERES OSR	0.780	25.1 W m^{-2}	-2.50 W m^{-2}
NOAA OLR	0.664	22.8 W m^{-2}	10.4 W m^{-2}

atic contributions to the resulting uncertainty estimates. Comparisons with observations of TOA fluxes from the CERES instrument are particularly well suited for this purpose since CERES also flies aboard the TRMM satellite and therefore provides a dataset that is temporally and spatially matched to the other observations used in the present study [for more information on the objectives and characteristics of the CERES instrument see Wielicki et al. (1996)].

Estimates of OLR at 1.0° resolution for February 1998 are compared with CERES observations over the same period in Fig. 8. The CERES data are obtained by averaging data from the CERES ERBE-like Monthly Regional Averages (ES-9) product¹ over the entire month to avoid misinterpreting the effects of diurnal models employed in producing CERES monthly mean products as errors. Differences between our results and those from CERES may be loosely interpreted as “error estimates” with the caveat that the CERES data are not perfect themselves. All error estimates made in this way are therefore approximate but are assumed to provide a ballpark and independent assessment of the accuracy of our TOA results.

The correlation coefficient, root-mean-square difference, and bias between the two datasets is provided in the first row of Table 3. Given the large uncertainties expected in ice cloud boundaries, agreement is very good. The data correlate better than 96% and exhibit a bias of less than 1 W m^{-2} . Figure 8 indicates a slight positive bias in the present study relative to CERES at low OLR ($<235 \text{ W m}^{-2}$) suggesting that cloud in the vicinity of convection may be too low or optically too thin, consistent with the inherent lack of information regarding cloud-sized ice hydrometeors in the GPROF retrievals. On the tropic-wide mean, this warm bias is, however, cancelled by a small negative bias in clear-sky regions ($\text{OLR} > 275 \text{ W m}^{-2}$).

A similar comparison of outgoing shortwave radiation estimates from the present study and CERES is presented in Fig. 9 and the corresponding correlation coefficient, rms difference, and bias are summarized in the second row of Table 3. Agreement in shortwave flux estimates is not as good as in their longwave counterparts. The correlation between the shortwave datasets is less than 80% while rms differences are $\sim 23 \text{ W m}^{-2}$.

¹ These data were obtained from the NASA Langley Research Center Atmospheric Sciences Data Center.

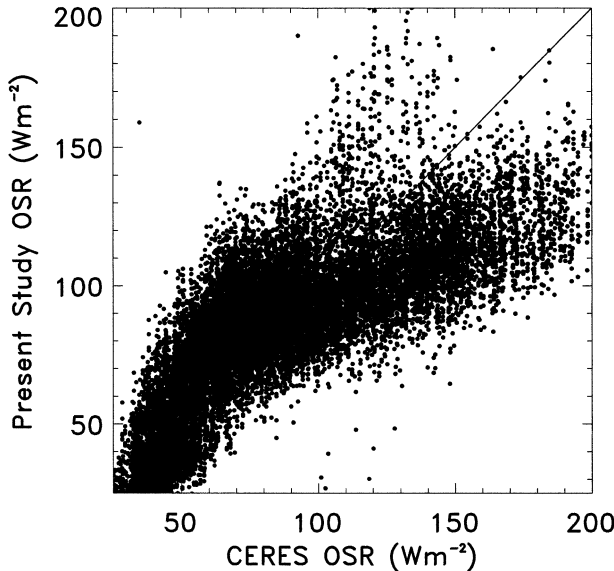


FIG. 9. As in Fig. 8 but for outgoing shortwave radiation (OSR).

Note, however, that the relative bias between the two datasets is less than 3 W m^{-2} due to a cancellation of overestimated reflection from nonprecipitating liquid clouds ($\text{OSR} < 100 \text{ W m}^{-2}$) and underestimated reflection from precipitation ($\text{OSR} > 100 \text{ W m}^{-2}$). The former may result from the albedo parameterizations used in BUGSrad overestimating the reflection due to nonprecipitating cirrus and stratus clouds or from systematic errors in LWP estimates. The latter can easily be explained by the fact that ice particles at the top of thick raining clouds are assumed to follow a monodispersed distribution with radius $100 \mu\text{m}$ consistent with assumptions in the GPROF database. In nature, particles at the tops of these clouds are much smaller resulting in significantly more reflection than is modeled in the present study.

For completeness, a comparison with the National Oceanic and Atmospheric Administration (NOAA) interpolated OLR product is provided in the last row of Table 3. (These data were provided by the NOAA-CIRES Climate Diagnostics Center, Boulder, Colorado, from their web site at <http://www.cdc.noaa.gov>.) Due to differences in the sampling of the Advanced Very High Resolution Radiometer (AVHRR) on the Geostationary Operational Environmental Satellites (GOES) from which the NOAA OLR product is derived and the TRMM satellite, both the correlation and rms differences are substantially worse relative to the comparison with CERES data. In fact, correlations between the NOAA and CERES products themselves are less than 70%. It is encouraging to note, however, that biases remain small ($\sim 10 \text{ W m}^{-2}$) suggesting that under-sampling by the TRMM satellite is substantially reduced when data are averaged to monthly timescales.

These results indicate that the bias component of the uncertainty is substantially less than the “worst case”

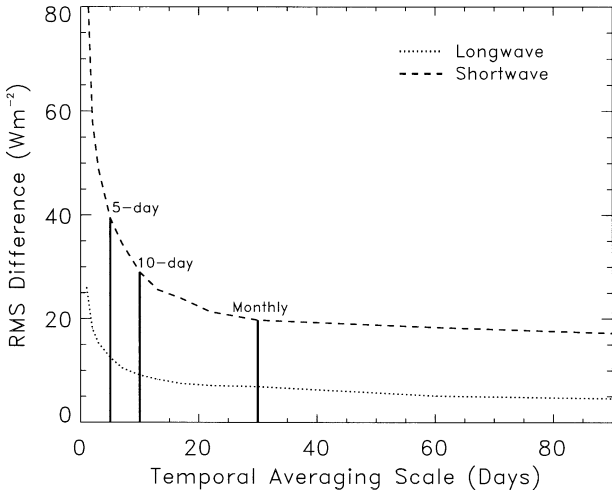


FIG. 10. Rms differences between outgoing longwave and shortwave radiation estimates at 1.0° resolution from the present study and the CERES ES-9 product. The leftmost data points correspond to instantaneous fluxes, while errors in 5-, 10-day, and monthly mean fluxes are highlighted for convenience.

total indicated by the sensitivity studies in the previous section. This is likely a result of both cancellation of competing sources of uncertainty and temporal averaging.

CERES data have also been used to probe the breakdown of the uncertainties in the present model into random and systematic components. Estimates of OLR and OSR are compared to CERES observations on a variety of different temporal scales in Fig. 10. On short timescales, these differences provide an estimate of the sum of random and bias errors while on longer scales, random errors, by definition, diminish through the averaging process leaving only the component owing to systematic biases. Uncertainties in instantaneous fluxes, represented by the 1-day averages in Fig. 10, are 27 and 80 W m^{-2} in OLR and OSR, respectively. At the other end of the spectrum, uncertainties in long-term means are 8 and 21 W m^{-2} . These results imply that random errors account for between 75% and 85% of the uncertainty in instantaneous fluxes, while the remainder must be due to systematic differences between the present work and the CERES product. Differences in 5- and 10-day, and monthly averages are highlighted for convenience. Random errors are also reduced through spatial averaging. Rms differences in 5° OLR and OSR estimates, however, are found to improve by only 10% relative to those at 1° resolution presented in Fig. 10.

In principle, the strong sensitivity of the current model to assumptions regarding cloud height, detection, and particle size provide a means for constraining the retrieval using broadband flux observations such as those made by CERES. While tempting, the possibility of calibrating the model by tuning parameters for better agreement with CERES is avoided for three reasons: 1) it eliminates CERES data as an independent source of

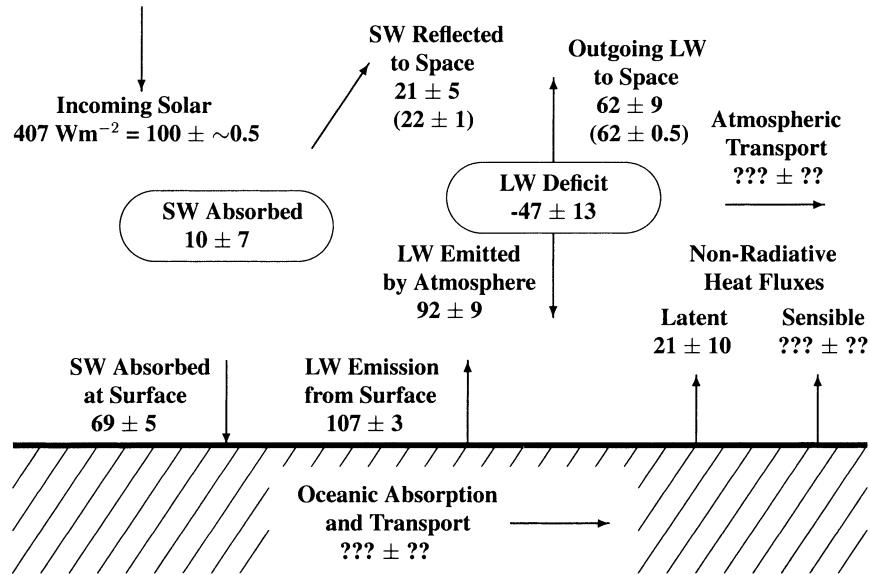


FIG. 11. Principal components of the tropical oceanic energy budget for Feb 1998. All fluxes have been normalized by the mean solar insolation at the top of the atmosphere, 407 W m^{-2} . Mean outgoing longwave and shortwave fluxes from CERES are provided in parentheses for comparison.

information for comparison purposes, 2) while we can make general arguments regarding the dominant sources of the errors in the technique, not all sources are known nor are their relative importance in the big picture so it is difficult to favor tuning one parameter over another, and (3) the tuning process may put too much confidence in the CERES estimates, which are themselves imperfect and could introduce additional biases in the results. As a result, no effort is made to force agreement between the two datasets at this time. To the contrary, these differences provide a useful source of additional information, which may prove invaluable in future applications to study cloud–radiation–climate interactions.

5. Discussion

A technique is described for generating tropic-wide (and ultimately global) estimates of the components of the energy budget over oceanic regions using explicit cloud and precipitation information from TRMM observations. These estimates in concert with the rigorous evaluation of their accuracy documented earlier are well suited to a wide variety of applications such as data assimilation, model validation, and studying climate variability. The results can, for example, be applied to study short-term climate variability through investigations of perturbations to the radiation balance induced by changes in the distributions of water vapor, cloud, and precipitation on short to moderate timescales, affording us the opportunity to quantify important relationships between the hydrologic cycle and the earth's energy budget.

The estimate of the short-term tropical oceanic energy

budget from TRMM observations in February 1998 illustrated in Fig. 11 provides a summary of the results that can be obtained using the method. In February 1998, the domain sampled by TRMM absorbs 40 W m^{-2} or 10% of the 407 W m^{-2} of solar radiation it receives. A further 85 W m^{-2} is reflected by atmospheric particles, clouds, and the surface, leaving 281 W m^{-2} to be absorbed by the ocean. At thermal wavelengths, it is found that the ocean emits 435 W m^{-2} of energy to the atmosphere while the atmosphere emits a total of 629 W m^{-2} , 376 W m^{-2} downward toward the surface and 253 W m^{-2} to space. Accounting for latent heat release, which amounts to an exchange of 82 W m^{-2} of energy from the surface to the atmosphere, the results imply a deficit of 72 W m^{-2} of energy in the atmosphere and a surplus of 140 W m^{-2} at the earth's surface. The implied net gain of 68 W m^{-2} in the earth–atmosphere system is consistent with the difference between the incoming solar radiation and emitted thermal radiation at the top of the atmosphere. It is speculated that these imbalances are largely accounted for by sensible heating, meridional energy transport, and absorption and transport of energy in the ocean. Finally, on average for the month of February 1998, the tropical atmosphere cools at -1 K day^{-1} and experiences a net cloud forcing of -8 W m^{-2} at TOA and -18 W m^{-2} at the surface.

A concerted effort has been made to characterize the uncertainty in all aspects of the approach. Uncertainty estimates derived from the sensitivity studies in section 4a are also summarized in Fig. 11. While errors in single pixels can be much larger, we anticipate uncertainties in regional-average (e.g., 10° resolution) longwave fluxes of at most 40 W m^{-2} due to a combination of errors

in water vapor, atmospheric temperature, and the distribution of ice cloud microphysical properties. Similarly, uncertainties in regional-average shortwave fluxes are not likely to exceed 40 W m^{-2} and are dominated by errors in prescribed surface albedo, errors in assessing the presence of low clouds, and ill-constrained liquid cloud microphysical properties. It should be noted that these estimates apply only to instantaneous flux calculations averaged over large spatial domains, errors in longer-term averages due to TRMM's once-a-day sampling have not been accounted for. Comparison with CERES observations suggests that temporal averaging substantially reduces these errors indicating uncertainties of less than 10 and 25 W m^{-2} , in monthly mean 1° by 1° longwave and shortwave fluxes, respectively.

Zhang et al. (1995) provide three important criteria governing the utility of a dataset for investigating cloud radiative effects:

- (1) they should cover the whole range of scales encompassing significant cloud variability, at least mesoscale (200 km , 3 hours) to planetary-climate scale ($10\,000 \text{ km}$, decade),
- (2) they should describe the shortwave and longwave radiative effects separately, and
- (3) they should describe variations of clouds, atmosphere, and surface properties separately.

As it is of considerable interest to investigate further the interactions between clouds, radiation, and precipitation, one might also add latent heating to the second point. This list provides a useful set of criteria by which to judge any climate-scale dataset. When applied to TRMM data and appropriate ancillary data from NWP model forecasts, the algorithm outlined in this paper is capable of providing a dataset that satisfies all of these requirements, with the exception of very short time-scales. Furthermore, the addition of microwave-based rainfall estimates make it possible to study the role of precipitation in the cloud–climate interaction problem. It is also important to note the potential for extending the application of the technique to the mesoscale and midlatitudes with data from follow-up missions such as the Global Precipitation Measurement (GPM) mission promise improved temporal resolution through the use of a constellation of satellites carrying TMI-like instruments.

By design, the technique presented above provides a framework for integrating observations of the global hydrologic cycle from a variety of sources to estimate their impact on the earth's energy budget that can be built upon as more accurate observations become available. One area of immediate concern is the large uncertainties in cloud and precipitation estimates over land surfaces due to their variable emissivities, the primary reason for their omission in the present work. Land areas play a significant role in global energy budget and hydrologic cycles, however, and need to be addressed. Further improvements to the flux estimates over both land and oceanic surfaces may be realized in the near future

through the next generation of observing systems, which seek to exploit synergies between active and passive observations to retrieve cloud and precipitation optical properties and their vertical distribution simultaneously to achieve consistency between distinct information sources.

Acknowledgments. Financial support for this research was provided, in part, by NASA TRMM Research Grant NAG5-7719 and by NASA Research Grant NAS5-99237. The development of BUGSrad has been supported by the U.S. Department of Energy under Contract DE-FG03-94ER61748. TRMM data was acquired through the Goddard Distributed Active Archive Center at the Goddard Space Flight Center. Water vapor, SST, and surface wind speed data used in the estimation of covariance matrices and radiative transfer calculations are produced by Remote Sensing Systems and sponsored, in part, by NASA's Earth Science Information Partnerships (ESIP): a federation of information sites for earth science; and by the NOAA/NASA Pathfinder Program for early EOS products, principal investigator: Frank Wentz. Interpolated OLR data were provided by the NOAA–Cires Climate Diagnostics Center, Boulder, Colorado, from their web site at <http://www.cdc.noaa.gov>. CERES data and ECMWF analyses were obtained from the NASA Langley Research Center Atmospheric Sciences Data Center.

REFERENCES

- Arking, A., 1991: The radiative effects of clouds and their impact on climate. *Bull. Amer. Meteor. Soc.*, **72**, 795–813.
- Ba, M. B., R. Frouin, S. E. Nicholson, and G. Dedieu, 2001a: Satellite-derived surface radiation budget over the African continent. Part I: Estimation of downward solar irradiance and albedo. *J. Climate*, **14**, 45–58.
- , S. E. Nicholson, and R. Frouin, 2001b: Satellite-derived surface radiation budget over the African continent. Part II: Climatologies of the various components. *J. Climate*, **14**, 60–76.
- Bishop, J. K. B., W. B. Rossow, and G. Ellsworth, 1997: Surface solar irradiance from the International Satellite Cloud Climatology Project 1983–1991. *J. Geophys. Res.*, **102**, 6883–6910.
- Breon, F.-M., R. Frouin, and C. Gautier, 1994: Global shortwave energy budget at the Earth's surface from ERBE observations. *J. Climate*, **7**, 309–324.
- Chen, T., W. B. Rossow, and Y. Zhang, 2000: Radiative effects of cloud-type variations. *J. Climate*, **13**, 264–286.
- Chen, T.-C., and M.-C. Yen, 1991: A study of the diabatic heating associated with the Madden–Julian oscillation. *J. Geophys. Res.*, **96**, 13 163–13 177.
- Cooper, S. J., T. S. L'Ecuyer, and G. L. Stephens, 2003: The impact of explicit cloud boundary information on ice cloud microphysical property retrievals from infrared radiances. *J. Geophys. Res.*, **108**, 4107, doi:10.1029/2002JD002611.
- Eyre, J. R., 1990: The information content of data from satellite sounding systems: A simulation study. *Quart. J. Roy. Meteor. Soc.*, **116**, 401–434.
- , G. A. Kelly, A. P. McNally, E. Anderson, and A. Persson, 1993: Assimilation of TOVS radiance information through one-dimensional variational analysis. *Quart. J. Roy. Meteor. Soc.*, **119**, 1427–1463.
- Fu, Q., and K.-N. Liou, 1992: On the correlated k -distribution method

- for radiative transfer in nonhomogeneous atmospheres. *J. Atmos. Sci.*, **49**, 2139–2156.
- Gill, A. E., 1980: Some simple solutions for heat-induced tropical circulation. *Quart. J. Roy. Meteor. Soc.*, **106**, 447–462.
- Goodberlet, M. A., C. T. Swift, and J. C. Wilkerson, 1989: Remote sensing of ocean surface winds with the Special Sensor Microwave/Imager. *J. Geophys. Res.*, **94**, 14 547–14 555.
- Greenwald, T. J., G. L. Stephens, T. H. Vonder Haar, and D. L. Jackson, 1993: A physical retrieval of cloud liquid water over the global oceans using special sensor microwave/imager (SSM/I) observations. *J. Geophys. Res.*, **98**, 18 471–18 488.
- Gupta, S. K., W. F. Staylor, W. L. Darnell, A. C. Wilber, and N. A. Ritchey, 1993: Seasonal variation of surface and atmospheric cloud radiative forcing over the globe derived from satellite data. *J. Geophys. Res.*, **98**, 20 761–20 778.
- Han, Q., W. B. Rossow, J. Chou, and R. M. Welch, 1998: Global survey of the relationships of cloud albedo and liquid water path with droplet size using ISCCP. *J. Climate*, **11**, 1516–1528.
- Harrison, E. F., P. Minnis, B. R. Barkstrom, V. Ramanathan, R. D. Cess, and G. G. Gibson, 1990: Seasonal variation of cloud radiative forcing derived from the Earth Radiation Budget Experiment. *J. Geophys. Res.*, **95**, 18 687–18 703.
- Hartmann, D. L., and D. A. Short, 1980: On the use of earth radiation budget statistics for studies of clouds and climate. *J. Atmos. Sci.*, **37**, 1233–1250.
- , H. H. Hendon, and R. A. Houze Jr., 1984: Some implications of the mesoscale circulation in tropical cloud clusters for large-scale dynamics and climate. *J. Atmos. Sci.*, **41**, 113–121.
- , M. E. Ockert-Bell, and M. L. Michelsen, 1992: The effect of cloud type on Earth's energy balance: Global analysis. *J. Climate*, **5**, 1281–1304.
- Hatzianastassiou, N., and I. Vardavas, 2001: Shortwave radiation budget of the Southern Hemisphere using ISSCP C2 and NCEP–NCAR climatological data. *J. Climate*, **14**, 4319–4329.
- Heckley, W. A., G. Kelly, and M. Tiedke, 1990: On the use of satellite-derived heating rates for data assimilation within the Tropics. *Mon. Wea. Rev.*, **118**, 1743–1757.
- Inoue, T., 1985: On the temperature and effective emissivity determination of semitransparent cirrus clouds by bispectral measurements in the 10 μm window region. *J. Meteor. Soc. Japan*, **63**, 88–98.
- Kasahara, A., and A. P. Mizzi, 1996: Use of precipitation data for diabatic initialization to improve the tropical analysis of divergence and moisture. *Meteor. Atmos. Phys.*, **60**, 143–156.
- King, M. D., Y. J. Kaufman, D. Tanré, and T. Nakajima, 1999: Remote sensing of tropospheric aerosols from space: Past, present, and future. *Bull. Amer. Meteor. Soc.*, **80**, 2229–2259.
- Knutson, T. R., K. M. Weickmann, and J. E. Kutzbach, 1986: Global-scale intraseasonal oscillations of outgoing longwave radiation and 250 mb zonal wind during Northern Hemisphere summer. *Mon. Wea. Rev.*, **114**, 605–623.
- Kummerow, C., and L. Giglio, 1994: A passive microwave technique for estimating rainfall and vertical structure information from space. Part I: Algorithm description. *J. Appl. Meteor.*, **33**, 3–18.
- , and Coauthors, 2000: The status of the Tropical Rainfall Measuring Mission (TRMM) after two years in orbit. *J. Appl. Meteor.*, **39**, 1965–1982.
- Lau, K.-M., and L. Peng, 1987: Origin of low-frequency (intraseasonal) oscillations in the tropical atmosphere. Part I: Basic theory. *J. Atmos. Sci.*, **44**, 950–972.
- L'Ecuyer, T. S., and G. L. Stephens, 2002: An uncertainty model for Monte Carlo retrieval algorithms: Application to the TRMM observing system. *Quart. J. Roy. Meteor. Soc.*, **128**, 1713–1737.
- Li, Z., H. G. Leighton, K. Masuda, and T. Takashima, 1993: Estimation of SW flux absorbed at the surface from TOA reflected flux. *J. Climate*, **6**, 317–330.
- Liebmann, B., and D. L. Hartmann, 1982: Interannual variations of outgoing IR associated with tropical circulation changes during 1974–1978. *J. Atmos. Sci.*, **39**, 1153–1162.
- Liou, K.-N., 1986: Influence of cirrus clouds on weather and climate processes: A global perspective. *Mon. Wea. Rev.*, **114**, 1167–1199.
- Madden, R. A., and P. R. Julian, 1972: Description of global-scale circulation cells in the tropics with a 40–50 day period. *J. Atmos. Sci.*, **29**, 1109–1123.
- Marshall, J. S., and W. H. Palmer, 1948: The distribution of raindrops with size. *J. Meteor.*, **5**, 165–166.
- Masunaga, H., T. Y. Nakajima, T. Nakajima, M. Kachi, R. Oki, and S. Kuroda, 2002: Physical properties of maritime low clouds as retrieved by combined use of Tropical Rainfall Measurement Mission Microwave Imager and Visible/Infrared Scanner: Algorithm. *J. Geophys. Res.*, **107** (D10), 4083, doi:10.1029/2001JD000743.
- McClatchey, F. A., R. W. Fenn, J. E. Selby, F. E. Volz, and J. S. Goring, 1972: Optical Properties of the Atmosphere. 3d ed. AFCLR-72-0497, Air Force Cambridge Research Laboratory, L. G. Hanscom Field, MA, 102 pp.
- Miles, N. L., J. Verlinde, and E. E. Clothiaux, 2000: Cloud droplet size distributions in low-level stratiform clouds. *J. Atmos. Sci.*, **57**, 295–311.
- Miller, B. I., 1962: On the momentum and energy balance of hurricane Helene (1958). National Hurricane Res. Project Rep. 53, U.S. Weather Bureau, Washington, DC, 19 pp.
- Miyahara, S., 1987: A simple model of the tropical intraseasonal oscillation. *J. Meteor. Soc. Japan*, **65**, 341–351.
- Moore, R. W., and T. H. Vonder Haar, 2001: Interannual variability of cloud forcing and meridional energy transport for the Northern Hemisphere winter from 1984–1990. *J. Climate*, **14**, 3643–3654.
- Olson, W. S., C. D. Kummerow, Y. Hong, and W.-K. Tao, 1999: Atmospheric latent heating distributions in the Tropics derived from satellite passive microwave radiometer measurements. *J. Appl. Meteor.*, **38**, 633–664.
- Palmén, E., and H. Riehl, 1957: Budget of angular momentum and energy in tropical cyclones. *J. Meteor.*, **14**, 150–159.
- Paltridge, G. W., 1980: Cloud-radiation feedback to climate. *Quart. J. Roy. Meteor. Soc.*, **106**, 895–899.
- Petty, G. W., 1990: On the response of the Special Sensor Microwave/Imager to the marine environment—Implications for atmospheric parameter retrievals. Ph.D. thesis, University of Washington, 291 pp.
- Prabhakara, C., R. S. Fraser, G. Dalu, M.-L. C. Wu, and R. J. Curran, 1988: Thin cirrus clouds: Seasonal distribution over oceans deduced from Nimbus-4 IRIS. *J. Appl. Meteor.*, **27**, 379–399.
- Puri, K., and N. E. Davidson, 1992: The use of infrared satellite cloud imagery data as proxy data for moisture and diabatic heating in data assimilation. *Mon. Wea. Rev.*, **120**, 2329–2341.
- Randel, D., and T. H. Vonder Haar, 1990: On the interannual variation of the earth radiation balance. *Nature*, **342**, 1168–1173.
- Riehl, H., and J. S. Malkus, 1961: Some aspects of Hurricane Daisy. *Tellus*, **13**, 181–213.
- Ringer, M. A., and K. P. Shine, 1997: Sensitivity of the Earth's radiation budget to interannual variations in cloud amount. *Climate Dyn.*, **13**, 213–222.
- Ritter, B., and J.-F. Geleyn, 1992: A comprehensive radiation scheme for numerical weather prediction models with potential applications in climate simulations. *Mon. Wea. Rev.*, **120**, 303–325.
- Rossow, W. B., and A. A. Lacis, 1990: Global, seasonal cloud variations from satellite radiance measurements. Part II: Cloud properties and radiative effects. *J. Climate*, **3**, 1204–1253.
- , and Y.-C. Zhang, 1995: Calculation of surface and top of the atmosphere radiative fluxes from physical quantities based on ISCCP data sets. 2. Validation and first results. *J. Geophys. Res.*, **100**, 1167–1197.
- Sassen, K., 2002: Cirrus: A modern perspective. *Cirrus*, D. K. Lynch et al., Eds., Oxford University Press, 11–40.
- Simpson, J., C. Kummerow, W.-K. Tao, and R. F. Adler, 1996: On the Tropical Rainfall Measuring Mission (TRMM). *Meteor. Atmos. Phys.*, **60**, 19–36.
- Slingo, A., and J. M. Slingo, 1988: The response of a general circulation model to cloud longwave radiative forcing. I: Intro-

- duction and initial experiments. *Quart. J. Roy. Meteor. Soc.*, **114**, 1027–1062.
- Slingo, J. M., and A. Slingo, 1991: The response of a general circulation model to cloud longwave radiative forcing. II: Further studies. *Quart. J. Roy. Meteor. Soc.*, **117**, 333–364.
- Sohn, B.-J., and E. A. Smith, 1992a: Global energy transports and the influence of clouds on transport requirements: A satellite analysis. *J. Climate*, **5**, 717–734.
- , and —, 1992b: The modulation of the low-latitude radiation budget by cloud and surface forcing on interannual time scales. *J. Climate*, **5**, 831–846.
- , and —, 1992c: The significance of cloud–radiative forcing to the general circulation on climate time scales—A satellite interpretation. *J. Atmos. Sci.*, **49**, 845–860.
- Somerville, R. C. J., and L. A. Remer, 1984: Cloud optical thickness feedbacks in the CO₂ retrieval problem. *J. Geophys. Res.*, **89**, 9668–9672.
- Stephens, G. L., 2002: Cirrus, climate, and global change. *Cirrus*, D. K. Lynch et al., Eds., Oxford University Press, 433–448.
- , and P. J. Webster, 1979: Sensitivity of radiative forcing to variable cloud and moisture. *J. Atmos. Sci.*, **36**, 1542–1556.
- , and T. J. Greenwald, 1991a: The Earth's radiation budget and its relation to atmospheric hydrology. 1. Observations of the clear sky greenhouse effect. *J. Geophys. Res.*, **96**, 15 311–15 324.
- , and —, 1991b: The Earth's radiation budget and its relation to atmospheric hydrology. 2. Observations of cloud effects. *J. Geophys. Res.*, **96**, 15 325–15 340.
- , G. G. Campbell, and T. H. Vonder Haar, 1981: Earth radiation budgets. *J. Geophys. Res.*, **86**, 9739–9760.
- , S.-C. Tsay, J. P. W. Stackhouse, and P. J. Flatau, 1990: The relevance of the microphysical and radiative properties of cirrus clouds to climate and climatic feedback. *J. Atmos. Sci.*, **47**, 1742–1753.
- , P. M. Gabriel, and P. T. Partain, 2001: Parameterization of atmospheric radiative transfer. Part I: Validity of simple models. *J. Atmos. Sci.*, **58**, 3391–3409.
- Takahashi, M., 1987: A theory of the slow phase speed of the intra-seasonal oscillation using the Wave-CISK. *J. Meteor. Soc. Japan*, **65**, 43–49.
- Tao, W.-K., S. Lang, J. Simpson, and R. Adler, 1993: Retrieval algorithms for estimating the vertical profiles of latent heat release: Their applications for TRMM. *J. Meteor. Soc. Japan*, **71**, 685–700.
- , and Coauthors, 2001: Retrieved vertical profiles of latent heat release using TRMM rainfall products for February 1998. *J. Appl. Meteor.*, **40**, 957–982.
- Toon, O. B., and J. B. Pollack, 1976: A global average model of atmospheric aerosols for radiative transfer calculations. *J. Appl. Meteor.*, **15**, 225–246.
- Vonder Haar, T. H., and V. E. Suomi, 1971: Measurements of the Earth's radiation budget from satellites during a five-year period. Part 1: Extended time and space means. *J. Atmos. Sci.*, **28**, 305–314.
- Weickmann, K. M., G. R. Lussky, and J. E. Kutzbach, 1985: Intra-seasonal (30–60 day) fluctuations of outgoing longwave radiation and 250 mb streamfunction during northern winter. *Mon. Wea. Rev.*, **113**, 941–961.
- Wentz, F., 1997: A well-calibrated ocean algorithm for special sensor microwave/imager. *J. Geophys. Res.*, **102**, 8703–8718.
- , C. Gentemann, D. Smith, and D. Chelton, 2000: Satellite measurements of sea surface temperature through clouds. *Science*, **288**, 847–850.
- Wielicki, B. A., B. R. Barkstrom, E. F. Harrison, R. B. Lee III, G. L. Smith, and J. E. Cooper, 1996: Clouds and the Earth's Radiant Energy System (CERES): An Earth Observing System experiment. *Bull. Amer. Meteor. Soc.*, **77**, 853–868.
- , and Coauthors, 2001: Evidence for large decadal variability in the tropical mean radiative energy budget. *Science*, **295**, 841–844.
- Willson, R. C., 1984: Measurements of solar total irradiance and its variability. *Space Sci. Rev.*, **38**, 203–242.
- Yanai, M., 1961: Dynamical aspects of typhoon formation. *J. Meteor. Soc. Japan*, **39**, 283–309.
- , S. Esbensen, and J.-H. Chu, 1973: Determination of bulk properties of tropical cloud clusters from large-scale heat and moisture budgets. *J. Atmos. Sci.*, **30**, 611–627.
- Yang, S., and E. A. Smith, 1999a: Four-dimensional structure of monthly latent heating derived from SSM/I satellite measurements. *J. Climate*, **12**, 1016–1037.
- , and —, 1999b: Moisture budget analysis of TOGA COARE area using SSM/I-retrieved latent heating and large-scale Q₂ estimates. *J. Atmos. Oceanic Technol.*, **16**, 633–655.
- , and —, 2000: Vertical structure and transient behavior of convective-stratiform heating in TOGA COARE from combined satellite-sounding analysis. *J. Appl. Meteor.*, **39**, 1491–1513.
- Zhang, Y.-C., W. B. Rossow, and A. A. Lacis, 1995: Calculation of surface and top of the atmosphere radiative fluxes from physical quantities based on ISCCP data sets. 1. Method and sensitivity to input data uncertainties. *J. Geophys. Res.*, **100**, 1149–1165.